International Journal of Greenhouse Gas Control 81 (2019) 170–180

Contents lists available at ScienceDirect

International Journal of Greenhouse Gas Control

journal homepage: www.elsevier.com/locate/ijggc

Gas Switching Reforming (GSR) for syngas production with integrated CO_2 capture using iron-based oxygen carriers

Abdelghafour Zaabout[a,*], Paul Inge Dahl[b], Ambrose Ugwu[c], Julian R. Tolchard[b], Schalk Cloete[a], Shahriar Amini[a,c]

[a] Sintef Industry, Process Technology Department, Norway
[b] Sintef Industry, Sustainable Energy Conversion Department, Norway
[c] Energy and Process Technology Department, NTNU, Norway

ARTICLE INFO

Keywords:
Chemical looping reforming
Gas switching reforming
Standalone fluidized bed
Iron-based oxygen carrier
Autothermal operation

ABSTRACT

The process behavior of a Gas Switching Reforming (GSR) reactor was studied using three different iron-based oxygen carrier materials: Iron-oxide on Alumina, Iron-Nickel oxide on Alumina and Iron-Ceria on Alumina. It was observed that, for all oxygen carriers, the fuel stage reaction occurs in two distinct sub-stages when feeding methane and steam to a bed of oxidized material, with methane combustion dominating the first and methane reforming dominating the second. This reflects a change in the catalytic activity of the oxygen carrier as it is reduced. The alumina support was observed to play a significant role in the reactions occurring, with the redox-active phases being hematite-structured Fe_2O_3 (oxidized form) and spinel-structured $(FeNiAl)_3O_4$ (reduced form).

The Nickel-containing oxygen carrier outperformed the others in the reforming sub-stage, showing 40% improved methane conversion. The feed of dry methane only during the combustion sub-stage was found to improve methane conversion to syngas in the subsequent reforming sub-stage from 75% to 80% at 800 °C. Results also show that methane conversion improves with the increase in operating temperature and steam/carbon ratio. Autothermal operation of the reactor was achieved with repeatable performance over several redox cycles. The study therefore successfully demonstrated autothermal N_2-free syngas production with integrated CO_2 capture from the fuel combustion required to supply heat to the endothermic reforming reactions.

1. Introduction

According to the latest IPCC report (IPCC, 2014), Carbon capture, utilization and storage, CCUS, will play a major role in cost effective mitigation of climate change caused by anthropogenic CO_2 emissions while meeting to the growing global energy demand. Tremendous research efforts have been deployed to applying CCUS to a wide spectrum of industrial applications covering power production (Viebahn et al., 2015; Rubin et al., 2012; Cormos et al., 2018) and CO_2 intensive industries (Cormos et al., 2018; Leeson et al., 2017; Bains et al., 2017).

CCUS can have a major impact in decarbonization of fossil fuel to in the form of clean hydrogen production. Natural gas reforming remains the main source for hydrogen (Barreto et al., 2003; Johnston et al., 2005), but the reforming process involves large CO_2 emissions due to the heat requirement for the highly endothermic methane reforming reaction, being supplied by fossil fuel combustion. Development of environmentally-friendly and cost-effective hydrogen production technologies from natural gas is, therefore, the key to fulfill the expected increasing demand for hydrogen while avoiding the potentially catastrophic consequences of self-strengthening global warming.

Chemical looping reforming (CLR) has emerged as a promising technology with minimal energy penalty for CO_2 capture from natural gas reforming (Ryden and Lyngfelt, 2006; Ryden et al., 2006). It is based on the so-called chemical looping combustion technology, CLC, where the difference is the final product being syngas (CO and H_2) for CLR, instead of heat in the case of CLC (Ryden and Lyngfelt, 2006; Ryden et al., 2006). The conventional CLR reactor configuration uses two interconnected fluidized bed reactors, namely the air and fuel reactors, where the oxygen carrier circulates between them transferring oxygen from air to the fuel, thereby avoiding any N_2 dilution of the produced syngas (Proell et al., 2010) (Fig. 1 shows a simplified scheme of the working principle of the CLR process). The heat from the highly exothermic oxidation reaction that takes place in the air reactor is transported by the oxygen carrier to the fuel reactor to be used mainly

* Corresponding author.
E-mail address: Abdelghafour.zaabout@sintef.no (A. Zaabout).

https://doi.org/10.1016/j.ijggc.2018.12.027
Received 9 September 2018; Received in revised form 20 December 2018; Accepted 27 December 2018
Available online 06 January 2019

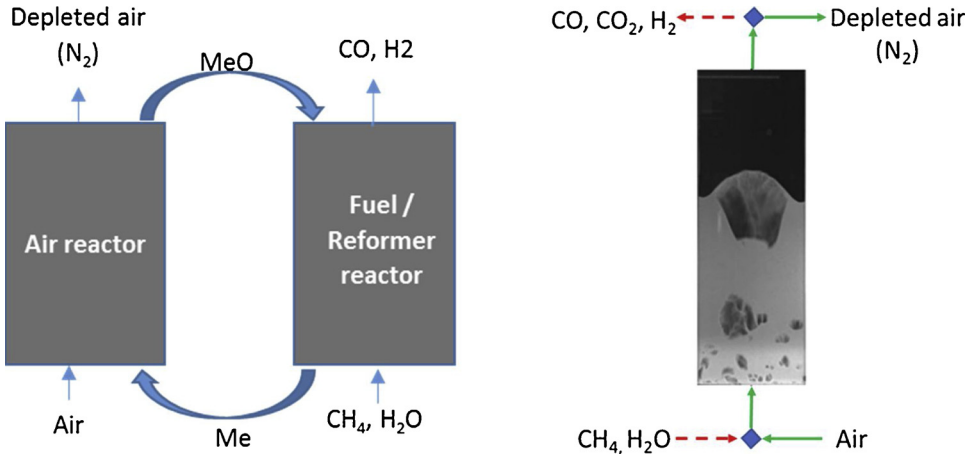

Fig. 1. Autothermal chemical looping reforming for syngas production with integrated CO_2 capture: a) simplified scheme of aCLR process and b) the working principle of the Gas Switching reforming under investigation in this paper.

by the endothermic reforming reaction. Two main CLR based processes have been investigated in the literature, with the difference being the fuel reactor configuration: i) sCLR process where conventional steam methane reforming takes place in tubular reactor filled with nickel, inserted in the fuel reactor of a CLC used for providing heat (Ryden and Lyngfelt, 2006), and ii) autothermal CLR (referred to as aCLR) where the oxygen carrier plays the role of a catalyst for methane reforming (Ryden et al., 2006; Ortiz et al., 2010) and reduction and reforming takes place in the same reactor. aCLR (it will be referred to as CLR in the rest of the manuscript) has received the greatest attention due to the better heat integration and process simplification ensured by avoiding the presence of reformer tubes in the fuel reactor (Ryden et al., 2006; Proell et al., 2010; Ortiz et al., 2010). This process has also been extended to steam-CLR process for combined syngas and hydrogen production; CH_4 converts to syngas through a gas-solid while pure hydrogen is produced by the steam feed for oxidizing the oxygen carrier (Hafizi et al., 2016).

CLR in the interconnected reactors configuration was successfully demonstrated in lab (Ryden and Lyngfelt, 2006; Ryden et al., 2006; de Diego et al., 2009) and pilot scale (Proell et al., 2010) under atmospheric conditions. To the best of authors' knowledge, no pressurized CLR studies were completed in this configuration to date, despite the predicted benefits of such a technology; a thermodynamic assessment has indeed shown that a 5% increase in energy efficiency could be achieved if CLR is operated under pressurized conditions, mainly gained from the energy saving made in H_2 compression (Adanez et al., 2012). Scale-up and operation of interconnected pressurized circulating fluidized bed reactors will be challenging. Tightly controlled solids circulation between the two interconnected reactors is critical to fulfill the heat and mass balance of the chemical looping process, but the solids circulation rate is highly dependent on the hydrodynamics in both reactors, presenting an important challenge when scaling up to larger reactor sizes and higher pressures. In addition, each component (reactors, cyclones and loop seals) should be pressurized separately in its own pressure vessel. This will increase cost and complexity and could lead to instantaneous pressure imbalances between the reactors that induce instabilities in solids circulation that could result in large leakages through the sealing devices and upset the reactor mass and energy balances.

This need has prompted research into novel reactor concepts with the ability to operate under pressurized conditions. Alternative reactor configurations proposed in the literature include moving bed (Tong et al., 2013), internally circulating bed (Zaabout et al., 2016), packed bed (Spallina et al., 2017) and gas switching technology (Zaabout et al., 2015; Wassie et al., 2017) (GST). The latter uses a cluster of reactors operating under bubbling/turbulent fluidization where oxidizing and reducing feed gases are alternated to each single reactor in the cluster (Zaabout et al., 2013) (Fig. 1 shows the working principle of GST applied to methane reforming). External solids circulation is therefore avoided, thereby greatly simplifying the reactor design and enabling operation under pressurized conditions (Wassie et al., 2018; Zaabout et al., 2017). GST is based on mature dense fluidized bed technology that is easy to operate and scale up. It has first been applied to combustion where several oxygen carriers have been tested, and shown successful autothermal operation of the concept (Zaabout et al., 2013, 2017). It was also successfully extended to methane reforming, through a concept called gas switching reforming (GSR), using a Ni-based oxygen carrier (Wassie et al., 2017) that has good reactive characteristics both in oxidation with air and reduction with methane, in addition to good catalytic activity for methane reforming.

1.1. Oxygen carriers for CLR

Active research activities are ongoing for development of suitable oxygen carriers for chemical looping reforming. The most successful oxygen carriers to date are Ni-based oxygen carriers, given the high catalytic activity of nickel for methane reforming. Successful experimental operation of the CLR process with Ni-based oxygen carriers covers lab (Ryden et al., 2006; de Diego et al., 2009) and pilot scale (Proell et al., 2010) studies in interconnected fluidized bed reactors, packed bed reactor (Spallina et al., 2017) and GSR configuration under investigation in this study (Wassie et al., 2017). These oxygen carriers performed well under CLR conditions in atmospheric and pressurized operation (the pressurized study was however completed in small dense fluidized bed reactor under batch conditions (Ortiz et al., 2010)) and have shown high selectivity to CO and H_2.

Attempts have however been made in developing oxygen carriers other than nickel to find cheaper and environmentally sound oxygen carriers with high reactivity and selectivity towards syngas. Fe-, Mn- and Cu-based oxygen carriers were tested in a TGA under CLR conditions but resulted in high methane slippage and low selectivity to syngas (Zafar et al., 2006). $Fe_2O_3/MgAl_2O_4$ oxygen carriers tested in a gram scale fixed bed reactor have shown good reactivity with methane towards CO_2 and H_2O in the beginning of the reduction stage, but the selectivity shifted to H_2 and CO with advanced reduction level of the oxygen carrier (Rydén et al., 2008). Authors speculated that the first phase is controlled by combustion where Fe_2O_3 is reduced to Fe_3O_4, before the second period with the selectivity to H_2 and CO begins. In this latter study, the addition of 1 wt.% NiO improved both CH_4 reactivity and selectivity to H_2 and CO. Similar behavior was reported for Fe_2O_3/Al_2O_3 oxygen carriers. Perovskite Fe-based oxygen carriers were tested and have been shown to be suitable for chemical looping

reforming, achieving very high selectivity to H_2 and CO (Rydén et al., 2008). Several studies have looked at Ce-Fe solid oxides-based oxygen carriers. Oxygen mobility was intensified in these oxygen carriers by the Ce–Fe chemical interaction via formation of $CeFeO_3$, thereby greatly enhancing their reducibility by CH_4 and syngas selectivity (Li et al., 2011; Zhu et al., 2014). CeO_2 was also tested under CLR conditions, but performed better when doped with Fe (He et al., 2009). $LaFeO_3$ oxygen carrier performance increased by ˜80% when 10% CeO_2 was used as a support and also showed high stability oven the consecutive CLR cycles. The excellent performance was attributed to the formation of Ce^{3+} and Fe^{2+} that maximizes vacant sites for oxygen storage, which also provided a good resistance to carbon deposition (Zheng et al., 2017).

To conclude, Fe-based oxygen carriers seem to be promising candidates for the CLR application, and have shown good methane conversion and high selectivity to syngas. On this basis, the present study investigates the behavior of the GSR concept with iron based oxygen carriers. Three Fe_2O_3-based oxygen carriers were prepared by impregnation on an Al_2O_3 commercial support and tested in a lab scale reactor under fluidized bed conditions relevant to the GSR concept. Promising performance has been achieved as it will be shown in the results section. In addition to the introduction and conclusion sections, this paper has two other main sections: i) experimental set-up and GSR operation; ii) results and discussion.

2. Experimental setup and operation

2.1. Experimental setup

The experimental setup used in this study (Fig. 2) consists of a cylindrical reactor column of, 5 cm in diameter and 50 cm in height. The reactor was also equipped with a freeboard region, that has an expanding conic zone (from 5 cm in the lower end diameter to 10 cm in the top end), followed by a cylindrical part. The total height of the freeboard zone is 40 cm A porous plate with 20 µm mean pore diameter and 3 mm thickness was used as a gas distributor placed at the bottom of the reactor. Both the reactor body and distributor were made of Inconel 600 to withstand the harsh conditions of high temperature gas-solids reactive flows (up to 1000 °C). An external electrical heater surrounding the reactor was used to heat up the reactor to the targeted operating temperature. The system heater and reactor were insulated using 25 cm thickness insulation, combining blankets and vermiculate. The hot gases exiting the reactor were cooled down before being sent to the vent, using a heat exchanger installed at the reactor outlet.

Mass flow controllers from Bronkhorst BV were used for feeding the different gases to the reactor. A three-way valve was used to alternate reducing and oxidizing conditions in the reactor. Dry gases were sampled just after the heat exchanger and analyzed with an *ETG MCA 100 Syn* analyzer, to measure the gas composition. The temperature was measured in two positions in the reactor; at 2 and 20 cm above the gas distributor using two thermocouples inserted from the top. A differential pressure sensor was continuously monitoring the pressure difference between the inlet and outlet of the reactor to detect any solid particles loss from the reactor. A steam generator with a high precision water pump was used for controlled steam feed to the reactor.

All the measurement instruments and flow controlling devices were controlled through a Labview application. The Labview application was also used for logging of data.

2.2. Oxygen carrier

Spherical gamma-alumina particles from Sasol (Puralox SCCa 150/200) were applied for wet impregnation of concentrated aqueous ammonium iron(I) citrate solution (˜50 g/100 g water) aiming to form nanostructured iron oxide inside the mesoporous alumina structure after heat treatment. The iron precursor was partly substituted by nickel (II) nitrate hexahydrate and cerium(III) nitrate hexahydrate to form iron oxide-nickel oxide and iron oxide-cerium oxide composite structures. Homogenous distribution of the active metal oxides throughout the porous particles was obtained by wet impregnation with subsequent drying steps at 120 °C after each step up to a theoretical loading of ˜10 wt% metal oxide, followed by heat treatment for 5 h at 500 °C (60 °C/h) in ambient air. This procedure was repeated until a theoretical loading of the active elements (Fe, Ni and Ce) was 1:1 by weight compared to Al in the porous alumina structure. The theoretical Fe:Ni and Fe:Ce ratios were 2:1 by weight. After the final impregnation and heat treatment steps, the as produced particles were sieved (100 µm) to remove fines prior to further analysis and testing. Particle size distributions after sieving, as measured by light diffraction are presented in Fig. 3.

SEM/EDS analysis on particles after sieving indicated a homogenous distribution of the Fe, Ni and Ce throughout the porous alumina structure, as seen in Fig. 4. The measured loading of active elements were slightly lower than aimed for (Fe + Ni + Ce: Al ≈ 0.8 : 1 by weight). This reflects the loss of active material by sieving, in form of fines which are loosely deposited on the surface of the particles. The Fe:Ni and Fe:Ce ratios were found to be ˜2:1, as anticipated.

The BET surface areas of the produced Fe-Al_2O_3, Fe-Ni–Al_2O_3 and Fe-Ce–Al_2O_3 impregnated particles were measured to 102.9, 97.2 and 80.9 m^2/g, respectively. In comparison, the bare alumina support particles had a BET surface area of 206.0 m^2/g. The measured bulk density of the three-oxygen carrier, under well-tapped packing conditions, is 1350 kg/m3 (the constant density of the three oxygen carriers is understandable, given that the active content was maintained constant for the three oxygen carriers based on weight percent). The estimated minimum fluidization velocity U_{mf} (Grace, 1986) for a D_{50} of 150 µm as shown in Fig. 3, at an operating temperature of 800 °C and atmospheric pressure is ˜0.0089 m/s when air is used as a fluidizing agent (air density and viscosity at 800 °C and atmospheric pressure were used).

2.3. Reactor operation and performance under the GSR mode

The GSR concept operates in a cyclic mode by alternating air and fuel feeds to the reactor. In GSR autothermal operation, the reactor is first heated up externally to the target temperature before starting the gas switching mode. The heaters are then switched off to complete the autothermal cycling operation, starting with the fuel stage where a gaseous fuel is fed for a fixed amount of time called as the "fuel time". This stage combines both oxygen carrier reduction and methane reforming to syngas. A feed of air follows to oxidize back the reduced oxygen carrier following an exothermic reaction that builds up heat in the reactor. The generated heat is then being used in the subsequent fuel stage with mainly endothermic reactions (reduction and reforming). Five seconds purging with an inert gas is applied between the air and fuel stages to avoid direct contact between them in the feed pipes, thereby eliminating the risk of explosion. The GSR reactor performance was quantified based on CH_4 conversion and selectivity to H_2 and CO calculated following Eqs. 1–3 respectively (FCH_4, FH_2 and FCO are the molar flow rates of these species).

Experiments for each operating condition were completed for at least four redox cycles to ensure repeatability. Gas composition at the reactor outlet and reactor temperature were collected continuously and were used to evaluate the GSR performance.

CH_4 Conversion

$$\gamma_{CH_4} = \frac{FCH_{4,in} - FCH_{4,out}}{FCH_{4,in}} \quad (1)$$

H_2 Selectivity

$$S_{H_2} = \frac{FH_{2,out}}{\gamma_{CH_4}{}^{*}4FCH_{4,in}} \quad (2)$$

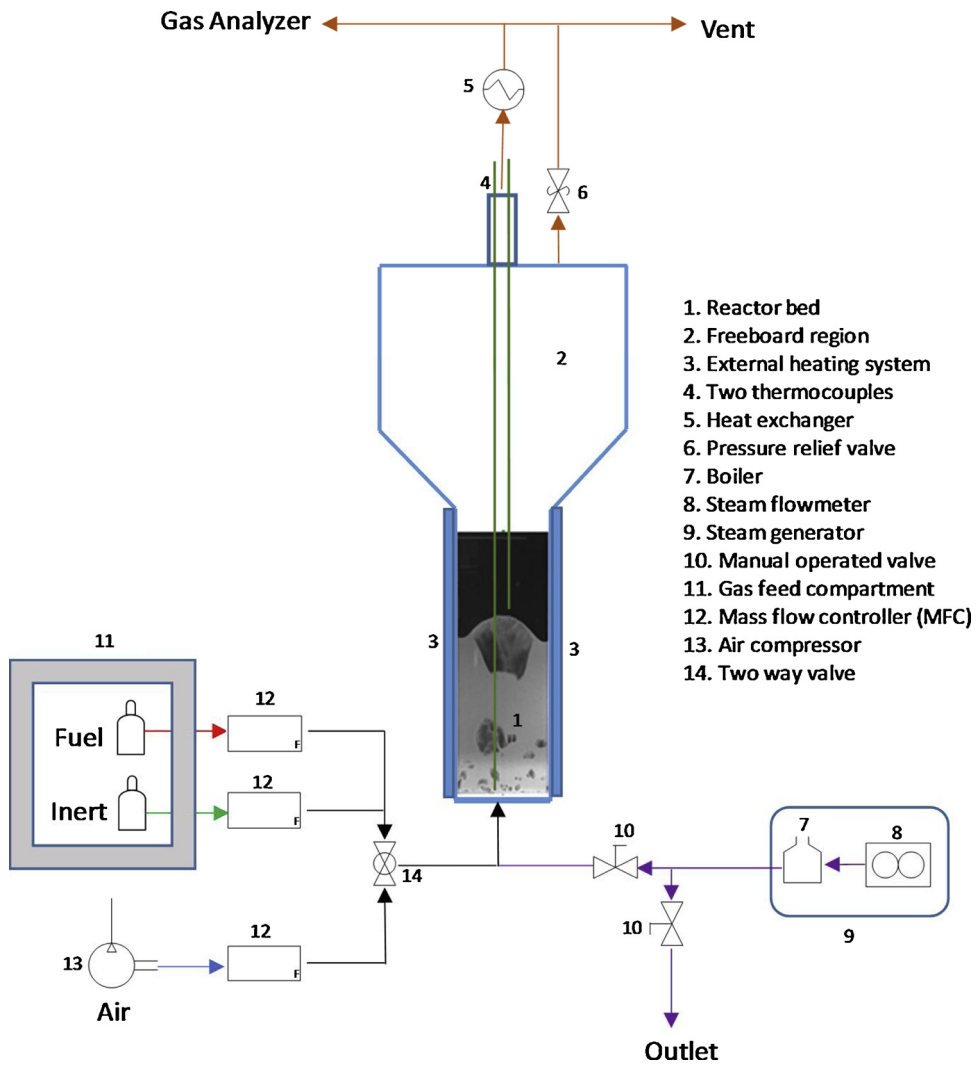

Fig. 2. A simple sketch of the experimental set up.

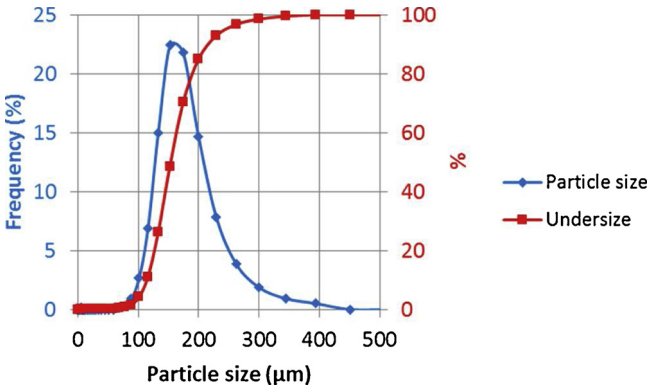

Fig. 3. Particle size distribution of impregnated supports.

CO Selectivity

$$S_{CO} = \frac{FCO_{out}}{\gamma_{CH_4}{}^{*}FCH_{4,in}} \quad (3)$$

3. Results

This section is organized as follows: the GSR behavior with the different iron-based oxygen carriers synthetized in the study is first shown. Afterwards, the GSR performance sensitivity to i) steam addition in the reduction stage, ii) the operating temperature, and iii) the steam per methane ratio, referred to as S/C. It should be noted that these experiments were completed with partial heat assistance, using the external heater, to compensate for the large heat losses taking place in the lab scale reactor over the range of investigated temperatures. This allowed exploring the GSR cycle behavior, with iron-based oxygen carriers, as it would happen in real industrial scale where heat losses will be minimal. Autothermal operation was completed lastly in optimal GSR conditions designed based on the outcome of the sensitivity study completed with external heat assistance. In all experiments, a mass of 286 g of oxygen carrier was initially placed in the reactor. With a CH_4 feed rate of 0.8 Nl/min, the corresponding specific solid inventory is 647. 15 kg/MW. The operating conditions of the different experiments completed in this study are reported in Table 1. The superficial gas velocities, U_g, were estimated in each GSR stage for each case study. It is worth mentioning that U_g was estimated for the maximum mole generation in each stage assuming full gas conversion (e.g. reforming of one mole CH_4 with two moles H_2O is assumed to generate one mole CO_2 and four moles H_2 resulting in a gas volume increase of 5/3).

3.1. GSR behaviour with iron-based oxygen carriers

GSR tests were completed on the three iron-based oxygen carriers

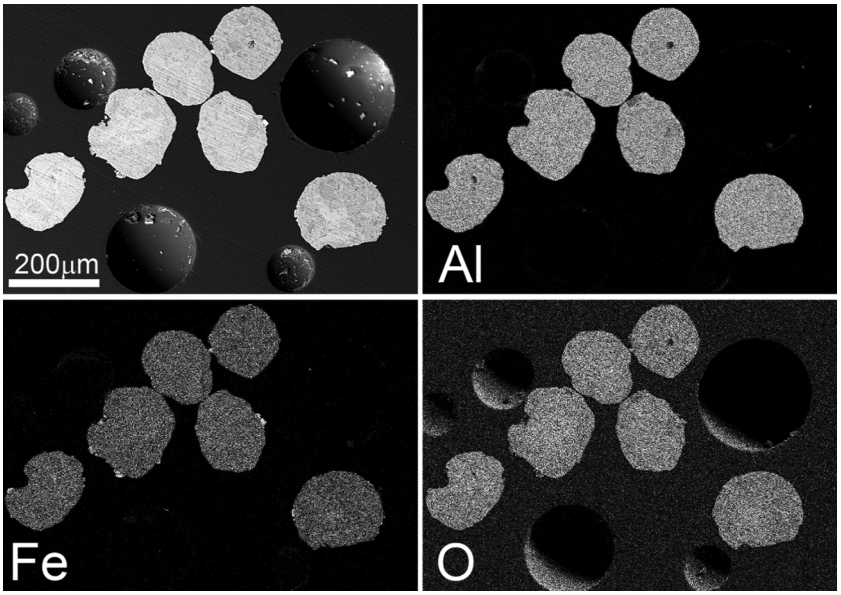

Fig. 4. SEM/EDS mapping analysis of impregnated alumina particles. The Backscattered electron image is shown in the top left, with corresponding Al, Fe and O maps.

using the same feed conditions at a target temperature of 800 °C and atmospheric pressure (Cases 1, 2 & 3 in Table 1). CH_4 and steam were fed in the fuel stage at an S/C = 2 (0.8 Nl/min CH_4 and 1.2 g/min water) for 12 min, while pure air was fed in the oxidation stage, at 10 Nl/min, for 3 min and 40 s (the oxygen carrier is brought back to almost full oxidation as can be seen on Fig. 5 showing a sharp increase of concentration O_2 in the outlet gas stream, just at the end of the oxidation stage).

The transient behaviour of the Fe-Al_2O_3 oxygen carrier over five GSR cycles is shown in Fig. 5. High conversion of CH_4 to CO_2 was achieved in the first half of the fuel stage, but decreases in the second half, showing high selectivity to syngas. Full conversion of oxygen was achieved over the entire oxidation stage, where oxygen comes out sharply only at the end of the oxidation stage. No carbon deposition was observed, as any deposited carbon would have been released in form of CO/CO_2 after being oxidized by the oxygen in the oxidation stage. This GSR cycle behaviour was very repeatable over the cycles as can be seen on Fig. 5.

The Fe-Ce-Al_2O_3 and Fe-Ni-Al_2O_3 have shown similar cycling behaviour as the Fe-Al_2O_3. Fig. 6 compares the achieved CH_4 conversion and selectivity to H_2 and CO for the three oxygen carriers. As found for the Fe-Al_2O_3, two distinct phases could also be identified for Fe-Ce-Al_2O_3 and Fe-Ni-Al_2O_3: complete conversion of methane to CO_2 is achieved in the first phase, while it drops to lower values in the second phase with high selectivity to syngas.

Methane conversion plots (Fig. 6a) shows the transition between the two phases to occur similarly for the Fe-Al_2O_3 and Fe-Ce-Al_2O_3 oxygen carriers, although it begins earlier for the latter (this is due to the significant reduction in the oxygen carrying capacity in the Fe-Ce-Al_2O_3 as CeO_2 did not contribute to the oxygen supply as shown by XRD analysis Fig. 8a)). This transition manifests by a drop in CH_4 conversion, but it continues in the combustion mode, where CH_4 converts to CO_2 and H_2O. Reforming of methane to syngas was found to occur only when methane conversion flattens out after the transition to show the very distinct phase 2. Interestingly, in the case of Fe-Ni-Al_2O_3, methane conversion drops substantially in the end of phase 1. This happened jointly with increased selectivity to H_2 and CO before methane conversion inversed to increase sharply and stabilize for the rest of the fuel stage. The different transitional behaviour of the Fe-Ni-Al_2O_3 oxygen carrier could be attributed to the presence of NiO that has to reduce to metallic Nickel before it starts catalysing the conversion of CH_4 to syngas (Zhou et al., 2013). It was expected that, at some reduction state of the oxygen carrier, combustion of methane by oxygen from NiO would create enough metallic nickel sites to catalyse significant methane reforming, but the results suggest that reforming activity starts only after the iron compounds in the oxygen carrier are also fully reduced. This could have resulted from the fact that nickel was part of the spinel as shown by the XRD analysis (Fig. 8).

Nevertheless, even though the transition between the two phases is not immediate for the Fe-Ni-Al_2O_3, it could safely be concluded that the fuel stage of the GSR concept, with the three iron-based oxygen carriers, comprises two distinct phases; one is dominated by combustion of methane while the second is dominated by methane reforming to syngas. Mass balance calculation of the reaction of CH_4 with Fe_2O_3

Table 1
Operating conditions of the different experiments completed in this study.

	Fe-Al_2O_3	Fe-Ce-Al_2O_3	Fe-Ni-Al_2O_3	Gas feed in reduction	S/C ratio in the reforming	T (°C)	$U_{g,air}$ (m/s)	$U_{g,red}$ (m/s)	$U_{g,ref}$ (m/s)
Case1	×			CH_4&H_2O	2	800	0.32	0.13	0.13
Case2		×		CH_4&H_2O	2	800	0.32	0.13	0.13
Case3			×	CH_4&H_2O	2	800	0.32	0.13	0.13
Case4			×	CH_4	2	800	0.32	0.075	0.13
Case5			×	CH_4	2	700	0.28	0.068	0.11
Case6			×	CH_4	2	750	0.3	0.071	0.12
Case7			×	CH_4	2	850	0.33	0.078	0.13
Case8			×	CH_4	1	800	0.32	0.075	0.099
Case9			×	CH_4	3	800	0.32	0.075	0.15
Case10			×	CO	2	850	0.47	0.28	0.34

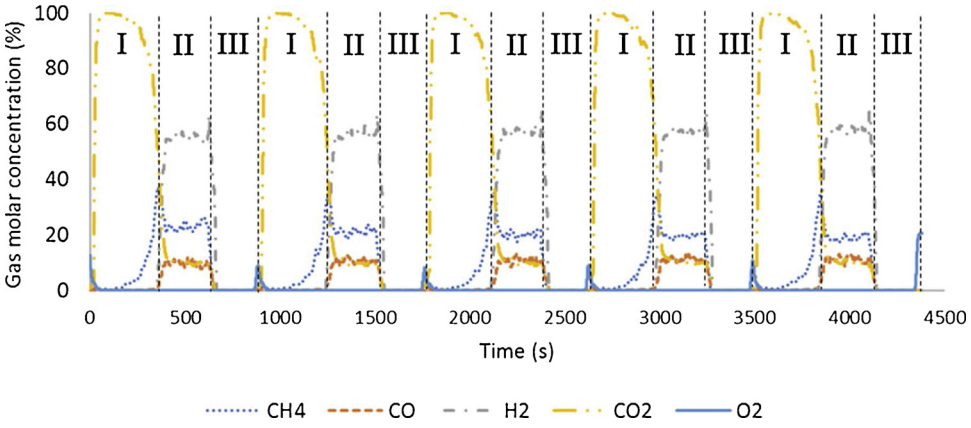

Fig. 5. Transient gas composition at the reactor outlet for five GSR cycles. Atmospheric operation pressure at 800 °C and S/C = 2 (0.8 Nl/min CH_4 and 1.2 g/min water) in the whole fuel stage. The GSR stages reduction, reforming and oxidation are numbered respectively I, II and III. The whole fuel stage time was 12 min and the oxidation time was 3 min and 40 s.

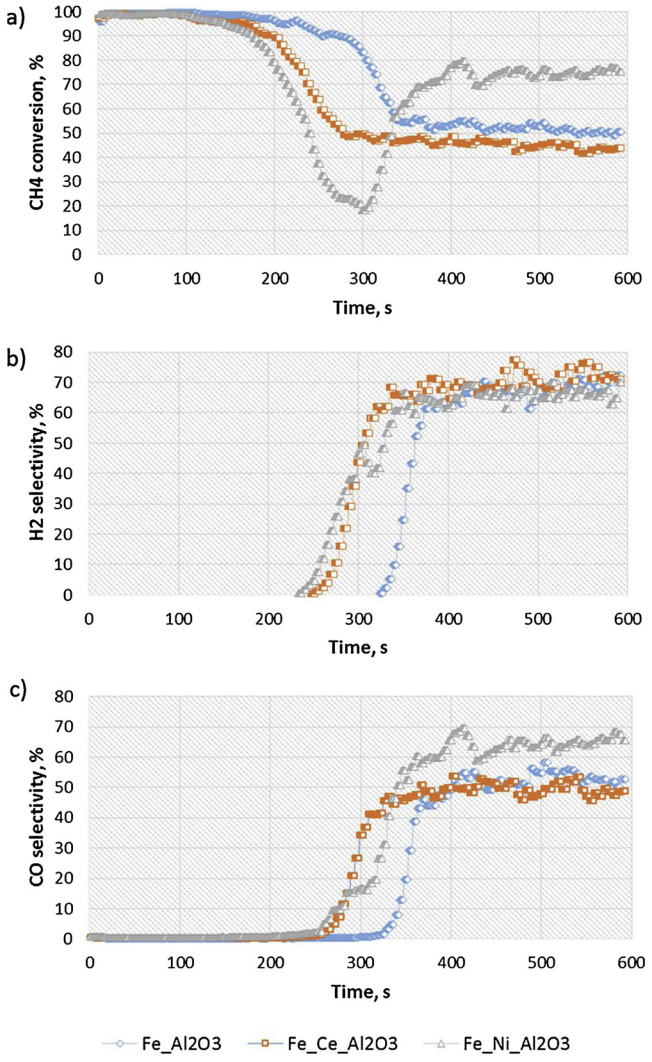

Fig. 6. Transient GSR performance in the fuel stage with Fe-Al_2O_3, Fe-Ce-Al_2O_3 and Fe-Ni-Al_2O_3 oxygen carriers. Atmospheric operation pressure at 800 °C and S/C = 2 (0.8 Nl/min CH_4 and 1.2 g/min water) in the whole fuel stage.

(assuming an ideal scenario where the oxygen carrier transitions between the different iron oxide states which are Fe_2O_3, Fe_3O_4, FeO and Fe) suggests that CH_4 converts well to CO_2 and H_2O over Fe_2O_3 and Fe_3O_4 to FeO. Indeed, for a mass of 286 g of the Fe-Al_2O_3 oxygen carrier, an active content of 35 wt.%, the total moles of Fe_2O_3 available for reaction is 0.35*286/159.7 = 0.63 mol. For a CH_4 feed rate of 0.8 Nl/min ˜288 s is needed to fully convert Fe_2O_3 to FeO. It can be seen on Fig. 6a) that full CH_4 conversion to CO_2 and H_2O occurs only in the first 200 s of the fuel stage (before it starts slowing down), corresponding to 70% of the time needed to fully convert Fe_2O_3 to FeO.

X-ray diffraction data for three samples after final stage reduction is presented Fig. 8, and an example of material after an oxidation step is presented in Fig. 7. It can be seen that the active oxidised phase in the Fe system is Fe_2O_3, and that at the temperatures of operation of 850 °C, the Al_2O_3 support has changed from a poorly crystalline transition alumina to be a relatively crystalline corundum-type α-alumina (Fig. 8). Some residual spinel phases are also evident (though not fitted), indicating incomplete reaction during the oxidation step.

The phases present after reduction are best understood as being solid solutions of spinel structured oxides of the general form M_3O_4, where M = Ni, Fe, or Al. It is important to note that in all these phases, iron is present as Fe^{2+} or as a mixture of Fe^{2+} and Fe^{3+}. There is no evidence of FeO, NiO or metallic Fe or Ni. For the Fe-Ce sample an additional CeO_2 phase is clearly also present and demonstrates a unit cell parameter in good accordance with literature values (a = 5.411 Å vs 5.410 Å (Pal'guev et al., 1959). Data fitting of the spinel component is presented in the form of three overlapping phases, though it is noted that there is complete solid-solubility in the Fe_3O_4-$NiFe_2O_4$-$NiAl_2O_4$-$FeAl_2O_4$ system, so this indicates a level of non-equilibrium.

The majority spinel phase in all samples after reduction (illustrated in red in Fig. 8) exhibits a unit cell parameter in the range 8.10 Å to 8.14 Å, consistent with an Al-rich Ni-Fe aluminate spinel (see supplementary plot S1). For the Fe-only system, the observed unit cell of a = 8.1337(1)Å is in close agreement with that of $FeAl_2O_4$ (Harrison et al., 1998). The Ni-Fe and Fe-Ce systems exhibit unit cell parameters smaller than those of $FeAl_2O_4$ though (a = 8.1131(1)Å and a = 8.1060(3)Å respectively). This confirms dissolution of Ni into the spinel phase in the Ni-Fe sample, and suggests a deviation from ideal M_3O_4 spinel stoichiometry towards a defective $Al_{2.66}O_4$ (γ-Al_2O_3 type)

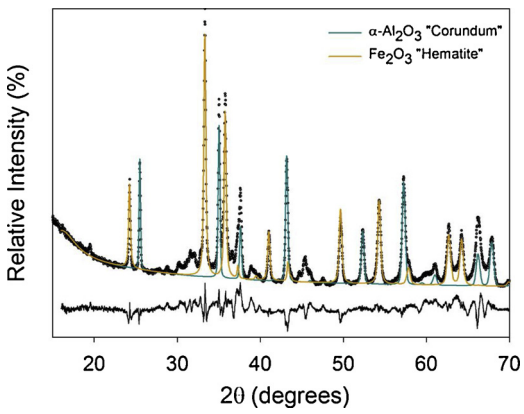

Fig. 7. A sample of Fe-Al_2O_3 following GSR cycling and oxidation at 850 °C.

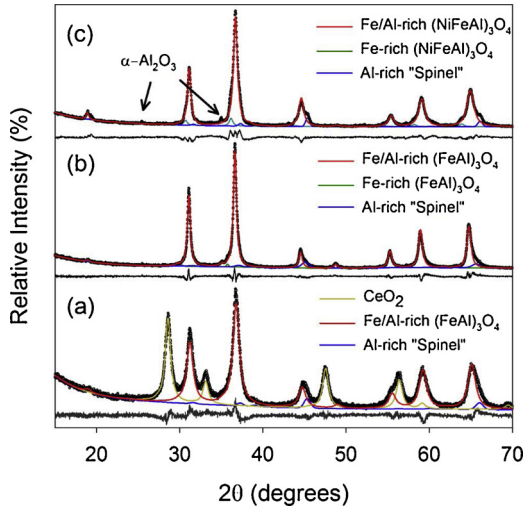

Fig. 8. Fitted XRD data for (a) A sample of Fe-Ce-Al_2O_3, after 30 min. final stage reduction at 800 °C, (b) a sample of Fe-Al_2O_3, after 30 min. final stage reduction at 800 °C, and (c) a sample of Fe-Ni-Al_2O_3, after 30 min. final stage reduction at 800 °C.

composition in the Fe-Ce system, as Ce does not readily form spinel structured solid solutions with Fe and Al.

The minority spinel phases observed are a phase with a unit cell parameter in the range a = 8.02 to 8.04 Å, and for the Fe and Ni-Fe systems a phase with unit cell parameter in the range a = 8.20 to 8.34 Å. The former of these is a defective γ-Al_2O_3 type phase, considering the published unit cell parameters for the Fe_3O_4-$NiFe_2O_4$-$NiAl_2O_4$-$FeAl_2O_4$ system (Harrison et al., 1998; Roelofsen et al., 1992; Quintanar et al., 1986; Wechsler et al., 1984). The latter is likely a Fe-rich / Alumina poor phase. Similar elements were found for 6 and 12 min fuel time on the Fe-Ni-Al_2O_3 (Fig. 9) suggesting that no further reduction of the oxygen carrier takes place when the reforming stage begins (it could be observed that the 6 min. data shows an additional phase than the 12 min., a result that could arise from the fact that the former was sampled after 8 days of operation, causing the sample to deactivate a bit).

Considering the XRD data, a simplified scheme for the redox cycling can be proposed:

Reduction reaction:

$$4Fe_2O_3 + 8Al_2O_3 + CH_4 \rightarrow 8FeAl_2O_4 + CO_2 + 2H_2O \quad (4)$$

Oxidation reaction:

$$2FeAl_2O_4 + 1/2O_2 \rightarrow Fe_2O_3 + 2Al_2O_3 \quad (5)$$

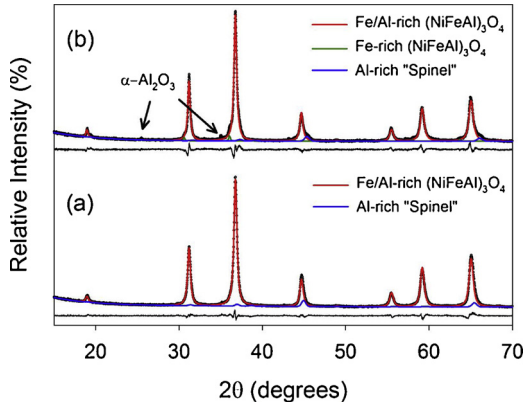

Fig. 9. Fitted XRD data for (a) A sample of Fe-Ni-Al_2O_3 following 6 min. reforming, and (b) following 12 min. reforming. Both at an operating temperature of 800 °C.

3.2. Mechanisms of Fe_2O_3 reduction with methane

On the light of the XRD results, the reduction stage (phase 1) occurs by reducing Fe_2O_3 to $FeAl_2O_4$ following an overall scheme resulting in methane combustion to CO_2. This is different from reaction scheme proposed by (Monazam et al. (2013)) for the reduction of Fe_2O_3 to FeO using methane based on TGA experiments, where the products contain CO_2, CO, H_2O and H_2 (Eq. 6).

$$7CH_4 + 27Fe_2O_3 \rightarrow 10Fe_3O_4 + 24FeO + 4CO_2 + 3CO + 6H_2O + 8H_2 \; \Delta H^0_{r,800C} = 1752.9\ \text{kJ/mol} \quad (6)$$

The reaction showing complete CH_4 conversion (Eq. 4) is expected to occur throughout both the reduction and reforming phases in the oxygen carriers not containing Ni. However, when the Fe_2O_3 reactant becomes depleted, the reaction slows down and significant fuel slip occurs.

Once the oxygen carrier becomes highly reduced, it becomes possible to complete oxidization with steam in the water splitting reaction (Eq. 7). It is not clear whether this reaction will produce Fe_2O_3, Fe_3O_4, or some intermediate Fe-Al-oxide, but it has been shown that the water splitting reaction happens when the oxygen carrier is highly reduced. In fact, this reaction has been isolated by feeding only steam to a fully reduced bed to achieve 40% conversion of steam to H_2 at 800 °C (See supplementary plot S2). Although it has not been explicitly confirmed, conversion of CO_2 to CO may also take place through the same mechanism (Eq. 8).

As shown in the earlier mol balance calculation, the production of H_2 and CO through these reactions become significant only when the oxygen carrier becomes almost completely reduced. Most likely, Eq. 7 starts producing H_2 earlier during the reduction phase, but the produced H_2 is converted back to steam over the excess Fe_2O_3 still present in the reactor. Substantial quantities of H_2 at the reactor outlet are only observed when the presence of Fe_2O_3 becomes very low. In addition, Fe-based materials are known to catalyse the water-gas shift reaction (Eq. 9), which further influences the H_2 to CO ratio in the produced syngas.

Through this mechanism, the Fe-Al_2O_3 and Fe-Ce-Al_2O_3 oxygen carriers behave like catalysts for steam methane reforming, although the reactions are not catalytic, but rather competing heterogeneous gas-solid reactions. The oxygen carrier is continuously reduced by the incoming methane fuel and the highly reduced oxygen carrier particles are oxidized by steam and CO_2 to form H_2 and CO. These reactions can continue indefinitely as long as heat is supplied to drive this endothermic reaction system.

$$2FeAl_2O_4 + H_2O \leftrightarrow Fe_2O_3 + 2Al_2O_3 + H_2 \quad (7)$$

$$2FeAl_2O_4 + CO_2 \leftrightarrow Fe_2O_3 + 2Al_2O_3 + CO \quad (8)$$

$$CO + H_2O \leftrightarrow CO_2 + H_2 \quad (9)$$

$$CH_4 + H_2O \leftrightarrow CO + 3H_2 \quad (10)$$

$$C + H_2O \leftrightarrow CO + H_2 \quad (11)$$

The substantial change in oxygen carrier behaviour for the Ni-containing material is signifies a change in mechanism to the catalytic steam-methane reforming reaction (Eq. 10). Even though no free Ni was observed in the XRD analyses, results suggest that the presence of Ni-compounds in the oxygen carrier still facilitates the steam-methane reforming reaction once the oxygen carrier becomes highly reduced.

However, the water splitting (Eq. 7) and CO_2 splitting (Eq. 8) reactions seem to be suppressed by the presence of Ni, as evidenced by the larger drop in methane conversion at the end of the reduction phase compared to the other two oxygen carriers. The operational challenge of this oxygen carrier is therefore to achieve a high degree of reduction to activate the catalytic steam-methane reforming reaction without excessive fuel slip in the reduction phase.

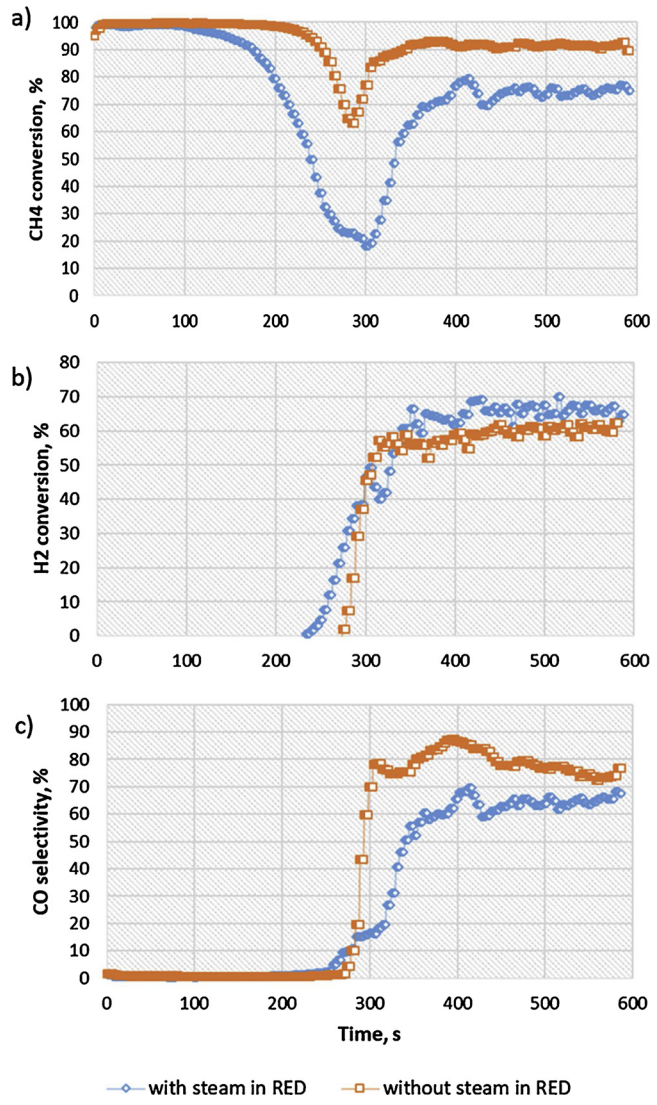

Fig. 10. Effect of steam addition in the reduction phase (the first 300 s of the fuel stage) on the GSR performance in the fuel stage. Atmospheric operation pressure at 800 °C and S/C = 2 (0.8 Nl/min CH_4 and 1.2 g/min water).

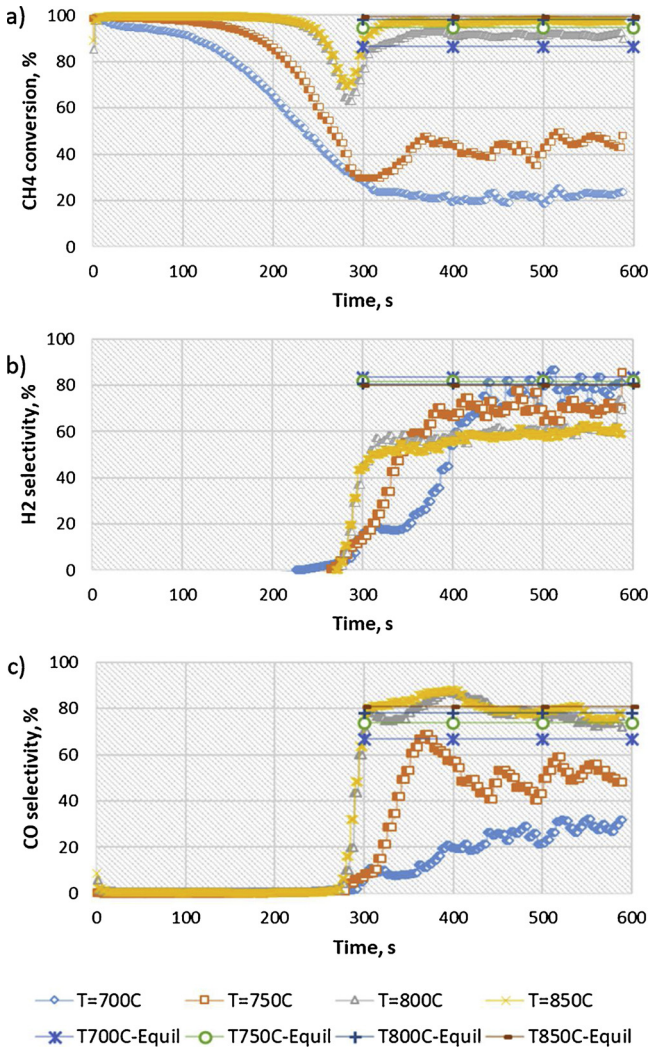

Fig. 11. Effect of operating temperature on the GSR performance in the fuel stage. Fe-Ni-Al2O3 oxygen carrier at atmospheric operation pressure. Dry methane was fed in the first 300 s (reduction phase), while steam was added to the last 300 s at S/C = 2 (0.8 Nl/min CH_4 and 1.2 g/min water). Equilibrium predictions were calculated assuming only steam methane conversion (Eq. 10) and water gas shift (Eq. 9) reactions taking place.

3.3. Sensitivity study

3.3.1. Effect of steam in the reduction stage

Methane is fully converted to CO_2 in phase 1 with all three oxygen carriers despite the presence of steam. Removing steam feed for this phase 1 would therefore allow substantial energy saving, if no negative side effects exist. In this respect, case 4 experiment was completed by feeding pure methane in phase 1 (first six minutes of the fuel time) while steam was only fed in phase 2 together with methane. Given the superior performance of the Ni-modified iron-based oxygen carrier in phase 2 dominated by methane reforming, this one was selected for the rest of the study.

As can be seen in Fig. 10. a), removing steam from phase 1 was found to have a very positive impact on methane conversion, leading to further prolonging the period with full methane conversion under the reduction mode in phase 1, and therefore reduces methane slippage in the transition to phase 2. This also delayed appearance of syngas in contrast to the case with steam feed, implying that presence of steam in phase 1 causes an earlier transition to syngas production.

Surprisingly, a large improvement in methane conversion to H_2 and CO occurs in phase 2 (over 90% methane conversion was achieved already at 800 °C), a result that could be attributed to the higher degree of reduction achieved by the pure methane feed. This has also affected the selectivity to hydrogen and CO, suggesting a change in the extents by which the different mechanisms contribute to syngas production.

A negative aspect of these results is that, some carbon deposition was detected in the form of a release of CO_2 in the oxidation stage. This CO_2 can only originate from the combustion of deposited carbon with oxygen in the air feed. Fortunately, this effect was quite small: the total released carbon in the oxidation stage was ˜1.1% of the total converted methane in the entire 12 min fuel stage.

3.3.2. Effect of temperature

This section compares cases 4, 5, 6 &7 (*Table* 1) to investigate the effect of the operating temperature. The GSR performance improves in both phase 1 and 2 with the operating temperature, with the largest impact being observed in phase 2 (dominated by the reforming). As can be seen on Fig. 11, good methane conversion was achieved in the beginning of phase 1 even at 700 °C. The extent of the complete methane conversion period increases with temperature, to cover more than 90% of phase 1 time at 850 °C.

In phase 2 dominated by methane reforming, methane conversion to syngas jumps from 20% at 700 °C to beyond 90% at 850 °C A

particularly large improvement takes place when increasing the temperature from 750 to 800 °C approaching equilibrium predictions (Fig. 11). This improvement could be attributed to the combined higher reduction degree of the oxygen carrier resulting from the prolonged high CH_4 conversion in phase 1 to CO_2 and H_2O, and the improved reaction kinetics. Appearance of H_2 and CO in phase 2 becomes sharper with increased temperature, thereby leading to faster transition between the combustion and reforming phases. This clear separation between the two phases is very beneficial for designing a GSR cycle with efficient fuel utilization (Nazir et al., 2018). For the 700 and 750 °C cases, the oxygen carrier is not fully reduced in the start of the reforming phase, thus delaying the onset of steady syngas production.

High amount of CO_2 release was detected in the air stage at 700 and 750 °C (~2.3% of converted methane in the entire fuel stage) but reduced to 1.1% at 800 °C and to 0.42% at 850 °C. This reflects existence of considerable methane cracking at these low operating temperature and explains the achieved high selectivity to H_2 at low temperature, as the carbon from the methane cracking ($CH_4 \leftrightarrow C + 2H_2$) remains on the oxygen carrier while H_2 leaves the reactor (Fig. 11). This tendency reduced with increasing temperature showing a decreased H_2 selectivity, while the CO selectivity jumped beyond equilibrium prediction (calculated assuming only steam methane reforming and water gas shift reactions taking place; Eq. 10 & Eq. 9) in the first half of the reforming phase at 800 and 850 °C, suggesting contribution of steam gasification of carbon (Eq. 11) to syngas production. The carbon gasification also explains the lower H_2 selectivity than equilibrium predictions at 800 and 850 °C (Fig. 11). Presence of steam gasification of deposited carbon from the beginning of the reforming phase suggests that carbon has already deposited in the reduction phase due to the feed of dry methane. Nevertheless, it is recommended to operate the reforming stage at temperatures above 800 °C to maximize methane conversion to syngas at acceptable slippage of carbon to the air stage.

3.3.3. Effect of steam-to-carbon ratio S/C

The effect of steam per carbon ratio, S/C, on the reforming phase performance was studied (cases 4, 8 & 9 in *Table* 1). Experiments were completed for three S/C, 1, 2 and 3. Pure methane was fed in phase 1 following the improved performance achieved across the whole GSR fuel stage, compared to the case with steam in phase 1 (case 3 in *Table* 1), as shown in the previous section.

As can be seen on Fig. 12.a), similar methane conversion in phase 1 was achieved for the three experiments, as pure methane was fed in each one. This means that the oxygen carrier achieves the same level of reduction for the three S/C values before the start of phase 2 where steam is added.

High methane conversion was achieved with no clear effect of S/C in phase 2; CH_4 conversion for S/C = 1 seems to be slightly lower in the second half of phase 2, but it remains relatively higher than equilibrium prediction for SMR reactions (Eq. 10 & Eq. 9), suggesting that other mechanisms contribute to syngas production (e.g. Eq. 7 and Eq. 8) that also led to lower H_2 selectivity than equilibrium. Obviously, excess of steam enhances selectivity to H_2, via the water gas shift reaction (Eq. 9) that is catalysed by both Ni and Fe compounds, but remains below equilibrium. Interestingly, although the increased S/C reduces CO selectivity as expected, it could clearly be seen that the achieved values are higher than equilibrium in the first half of the reforming phase for both S/C = 2 and 3 (for longer time at S/C = 3), reflecting contribution of steam gasification of deposited carbon to syngas production. This clearly explains the reduced extent of carbon slippage to the air stage with the extent of steam excess; from 1.3% at S/C = 1 to 0.76% at S/C = 3 (larger quantities of deposited carbon gasifies in the reforming phase as S/C is increased).

3.4. Autothermal operation with $Fe\_Ni\_Al_2O_3$

Experience from the prior experiments will now be used to operate

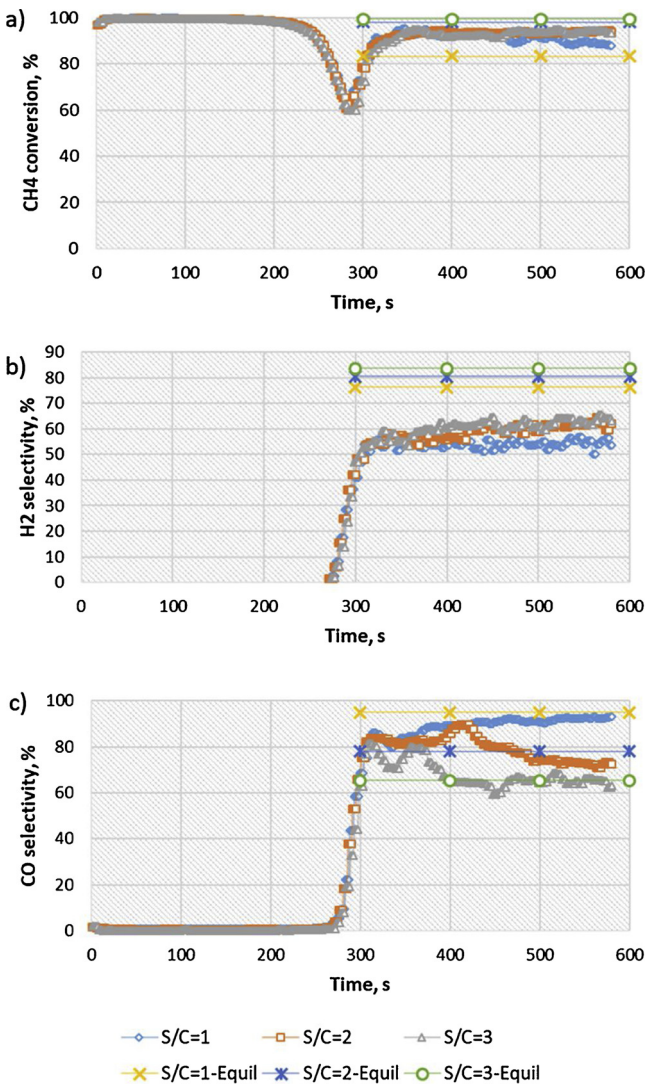

Fig. 12. Effect of steam per carbon ratio, S/C = 1, 2 & 3, on the GSR performance in the fuel stage. Fe-Ni-Al2O3 based oxygen carrier was used. Operating temperature of 800 °C at atmospheric pressure. Dry methane was fed in the first 300 s (reduction phase), while steam was added to the last 300 s at different S/C = 2 (reforming phase). Equilibrium predictions were calculated assuming only steam methane conversion (Eq. 10) and water gas shift (Eq. 9) reactions taking place.

the GSR cycle autothermally. In this experiment, no external heat was supplied to the reactor in any stage of the GSR cycle, but rather the cycle was designed in a way that the overall heat requirement (endothermic methane reforming reaction, heat removed by gases, in addition to heat losses from the reactor) is fulfilled by the exothermic reaction (mainly the oxidation of the oxygen carrier, but it could also be in the reduction stage if CO is used).

It is worth reminding that the GSR process with iron-based oxygen carrier was found to take place following three well defined stages; oxidation, reduction and reforming. The transition between the reduction and reforming stages could be completed with minimal fuel slippage if dry gaseous fuel is used in the reduction stage at sufficiently high temperature (Fig. 10), with steam feed added only in the reforming stage. The three-stage behaviour of the GSR process opens the possibility of using gaseous fuels other than methane in the reduction stage. This becomes especially interesting if hydrogen production is the final product, where PSA off-gas could be used as feed to the reduction phase. This GSR configuration has been proposed for H_2 production with integrated CO_2 capture (Wassie et al., 2017; Nazir et al., 2018;

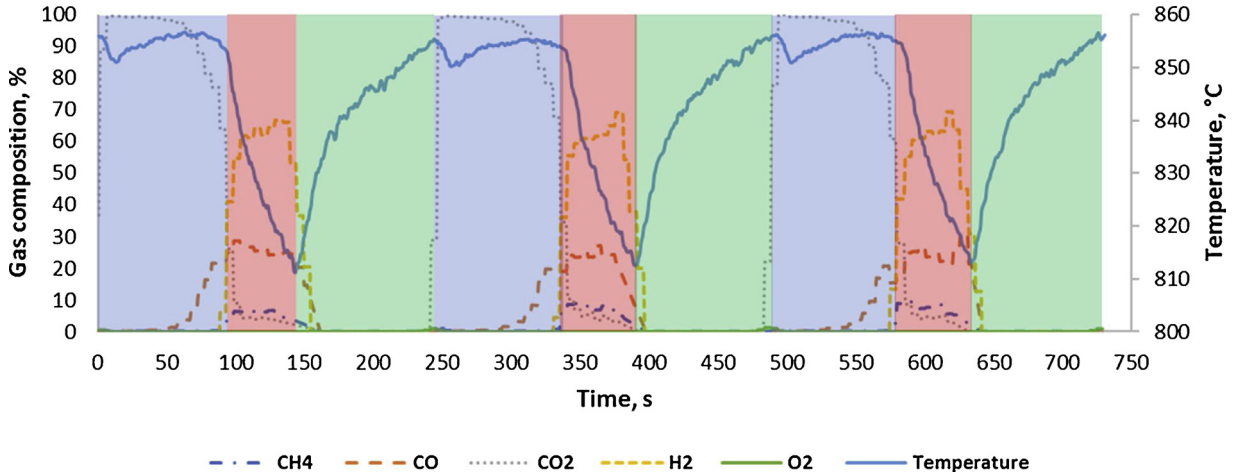

Fig. 13. Transient temperature and gas composition behaviour of autothermal operation of the three-stage GSR process with Fe-Ni-Al_2O_3 based oxygen carrier over three cycles. CO was fed in the reduction stage (9.6 Nl/min for 90 s), steam and CH_4 were fed in the reforming stage (2.4 Nl/min with S/C = 2, for 50 s) and air was fed in the oxidation stage (15 Nl/min for 120 s). Target temperature at the start of reduction stage is 850 °C and atmospheric operation pressure. Reduction stage in blue, reforming stage in red and oxidation stage in green (For interpretation of the references to colour in this figure legend, the reader is referred to the web version of this article).

Francisco Morgado et al., 2017). The presence of a high CO content in the off-PSA gasses gives another advantage to the reforming stage, owing to its exothermic reaction with the iron-based oxygen carrier that releases heat in the reduction, thereby allowing the subsequent reforming stage to start at a higher temperature than the case of methane which has an endothermic reduction reaction.

All combined, the autothermal operation was completed in optimal conditions following the three-stages GSR configuration (to avoid any confusion, the terminology "stage" is used in the rest of the manuscript instead of "phase"). Pure CO is fed in the reduction stage, steam and methane in the reforming stage, and air in the oxidation stage (case 10 in *Table* 1). The cycle starts with the reduction stage at a reactor temperature of ~850 °C for a reduction time designed to reach the same reduction level achieved in experiments shown in section 3.3.1. A reforming stage follows where the temperature drops due to the endothermic reaction, then the oxidation stage is applied where heat is built up again in the reactor, thereby bringing the temperature back to 850 °C for starting a new GSR cycle.

As can be seen in Fig. 13, the temperature in the reactor cycles well between 855 °C and ~810 °C by alternating the three GSR stages, demonstrating the ability of the three-stage GSR concept to run autothermally. In the reduction stage, complete conversion of CO was achieved in the two thirds of the stage, before it starts decreasing gradually towards the end of the stage. The exothermic reaction of CO with the oxygen carrier maintained the temperature high across the stage which allowed starting the reforming stage at a high temperature (855 °C). The reforming stage was stopped at a temperature of 810 °C, to avoid high methane slippage as shown in the previous section 3.3.2. Gas composition measurements confirm that high conversion of methane to syngas (~81.45%) is achieved across the entire reforming stage (Fig. 13), with an averaged H_2 production of ~2.39 mols and 0.95 mol of CO, for each converted mole of CH_4. This is below equilibrium prediction (~3.19 mol H_2/mole CH_4), confirming contribution of mechanisms other than SMR (Eq. 10) and WGS (Eq. 9) reactions in CH_4 conversion to syngas. The higher methane slippage compared to the case shown in Figs. 10 and 11, completed at similar range of temperature could be attributed to the methane feed rate which is three times higher in this autothermal operation experiment. Full conversion of oxygen was achieved in the entire oxidation stage demonstrating the high reactivity of the oxygen carrier with oxygen. It should also be emphasised that no CO_2 release was observed in the oxidation stage, thereby proving the absence of carbon deposition.

The aforementioned autothermal behaviour of the three-stage GSR configuration was repeatable over cycles, by alternating the gas feeds into the bed of iron-based oxygen carrier, thereby maintaining the bed temperature cycling between 855 and 810 °C.

Due to large heat losses from the lab-scale reactor, the length of the reforming stage was found to be ~2.2 times shorter than the theoretical prediction by heat balance calculation. The total CO feed to the reduction stage was ~0.59 mol, requiring ~1.38 mol of air to oxidize back the oxygen carrier. The total heat generated in the system from combustion of CO is then equal to ~157.7 kJ (assuming 95% CO conversion). This heat is used for heating up gases from room temperature to the reactor operating temperature for driving the endothermic steam-methane reforming reaction with an enthalpy of 206 kJ/mol. The calculated theoretical time of the reforming stage is ~110 s while the experimental one was only 50 s. With the achieved performance in the reforming stage, of 2.39 mol of H_2 and 0.95 mol of CO per mole of CH_4 converted (at ~81.45% conversion rate), the efficiency of syngas production (ratio of LHV of produced syngas and total LHV of fuel converted in the GSR cycle) in this lab scale reactor is only ~26.6% against 70% theoretically predicted for an industrial scale GSR assuming no heat losses and 83% with heat integration (Nazir et al., 2019). Given that the heat losses will be negligible in an industrial scale reactor, the GSR concept has the prospect to entirely remove the energy penalty for capturing CO_2 from SMR based hydrogen production.

4. Conclusion

An experimental campaign was completed to investigate the Gas Switching Reforming, GSR, process behaviour with iron-based oxygen carriers, for natural gas conversion to syngas with integrated CO_2 capture. Three iron-based oxygen carriers, prepared using impregnation of active materials on alumina support, were tested under relevant GSR conditions. The base case oxygen carrier was 35 wt.% hematite on alumina, while 10 wt.% of hematite was replaced by CeO_2 in the second, and by NiO in the third one.

The fuel stage, with CH_4 and steam feed, was found to occur following two separate sub-stages where methane combustion to CO_2 dominates in sub-stage 1, while high selectivity to syngas dominates in sub-stage 2. Syngas production has likely occurred with dominance of catalytic steam methane reforming route on the NiO doped oxygen carrier, while for the two other oxygen carriers, the reaction mechanism changes to a simultaneous Fe_2O_3 reduction with CH_4 to form CO_2 and

H_2O and partial oxidation of the oxygen carrier by H_2O and CO_2 to form H_2 and CO. This mechanism only becomes visible when the oxygen carrier becomes highly reduced so that there is almost no Fe_2O_3 left to oxidize the produced H_2 and CO. However, this mechanism could not achieve sufficiently high methane conversion, indicating that some Ni-content on the oxygen carrier will still be required in practical applications.

Dry methane feed over the Fe-Ni oxygen carrier improved methane conversion in both reduction and reforming sub-stages, but resulted in carbon deposition (1% from the total converted methane in the entire fuel stage) that was however observed in the form of CO_2 release in the beginning of the oxidation stage. Increased operation temperature has improved fuel conversion and reduced the extent of carbon slippage to the air stage, while the steam/carbon ratio had a minor effect on methane conversion.

A good performance has been achieved in GSR autothermal operation when CO was used in the reduction sub-stage, owing to the exothermic reduction reaction with CO. This further increase the attractiveness of GSR where the three-stages operation mode (reduction, reforming and oxidation) can maximize fuel conversion by using PSA-off gases in the reduction stage when pure hydrogen production is the final targeted product. It could therefore be safely concluded that operation of the GSR process with iron based oxygen carriers is possible at high methane conversion.

Acknowledgement

The authors would like to acknowledge the support from the European Commission under the NanoSim grant (project number: 604656) and SINTEF for the open access fees. VATL Lab technicians at the Norwegian University of Science and Technology are acknowledged for constructing and maintaining the experimental set up. The assistance of internship students Florent Gaimbaud and Olivier Planton in running experiments is also acknowledged.

Appendix A. Supplementary data

Supplementary material related to this article can be found, in the online version, at doi:https://doi.org/10.1016/j.ijggc.2018.12.027.

References

Adanez, J., et al., 2012. Progress in chemical-looping combustion and reforming technologies. Prog. Energy Combust. Sci. 38 (2), 215–282.
Bains, P., Psarras, P., Wilcox, J., 2017. CO2 capture from the industry sector. Prog. Energy Combust. Sci. 63, 146–172.
Barreto, L., Makihira, A., Riahi, K., 2003. The hydrogen economy in the 21st century: a sustainable development scenario. Int. J. Hydrogen Energy 28 (3), 267–284.
Cormos, A.M., et al., 2018. Carbon capture and utilisation technologies applied to energy conversion systems and other energy-intensive industrial applications. Fuel 211, 883–890.
de Diego, L.F., et al., 2009. Hydrogen production by chemical-looping reforming in a circulating fluidized bed reactor using Ni-based oxygen carriers. J. Power Sources 192 (1), 27–34.
Francisco Morgado, J., et al., 2017. Modelling study of two chemical looping reforming reactor configurations: looping vs. switching. Powder Technol. 316, 599–613.
Grace, J., 1986. Contacting modes and behaviour classification of gas–solid and other two-phase suspensions. Can. J. Chem. Eng. 64 (3), 353–363.
Hafizi, A., Rahimpour, M.R., Hassanajili, S., 2016. Hydrogen production via chemical looping steam methane reforming process: effect of cerium and calcium promoters on the performance of Fe2O3/Al2O3 oxygen carrier. Appl. Energy 165, 685–694.
Harrison, R.J., Redfern, S.A.T., O'Neill, H.S.C., 1998. Am. Mineral. 83, 1092–1099.
He, F., et al., 2009. Synthesis gas generation by chemical-looping reforming using Ce-Based oxygen carriers modified with Fe, Cu, and Mn oxides. Energy Fuels 23 (3-4), 2095–2102.
IPCC, 2014. Climate Change Mitigation: Summary for Policymakers.
Johnston, B., Mayo, M.C., Khare, A., 2005. Hydrogen: the energy source for the 21st century. Technovation 25 (6), 569–585.
Leeson, D., et al., 2017. A Techno-economic analysis and systematic review of carbon capture and storage (CCS) applied to the iron and steel, cement, oil refining and pulp and paper industries, as well as other high purity sources. Int. J. Greenh. Gas Control. 61, 71–84.
Li, K.Z., et al., 2011. Transformation of methane into synthesis gas using the redox property of Ce-Fe mixed oxides: effect of calcination temperature. Int. J. Hydrogen Energy 36 (5), 3471–3482.
Monazam, E.R., et al., 2013. Kinetics of the reduction of hematite (Fe2O3) by methane (CH4) during chemical looping combustion: a global mechanism. Chem. Eng. J. 232, 478–487.
Nazir, S.M., et al., 2018. Techno-economic assessment of the novel gas switching reforming (GSR) concept for gas-fired power production with integrated CO2 capture. Int. J. Hydrogen Energy.
Nazir, S.M., et al., 2019. Gas switching reforming (GSR) for power generation with CO2 capture: process efficiency improvement studies. Energy 167, 757–765.
Ortiz, M., et al., 2010. Hydrogen production by auto-thermal chemical-looping reforming in a pressurized fluidized bed reactor using Ni-based oxygen carriers. Int. J. Hydrogen Energy 35 (1), 151–160.
Pal'guev, S.F., Alyamovskii, S.I., Volchenkova, Z.S., 1959. Russ. J. Inorg. Chem. 4, 1185–1188.
Proell, T., et al., 2010. Syngas and a separate nitrogen/argon stream via chemical looping reforming - A 140 kW pilot plant study. Fuel 89 (6), 1249–1256.
Quintanar, C., et al., 1986. J. Magn. Magn. Mat. 54/57, 1339–1340.
Roelofsen, J.N., Peterson, R.C., Raudsepp, M., 1992. Am. Mineral. 77, 522–528.
Rubin, E.S., et al., 2012. The outlook for improved carbon capture technology. Prog. Energy Combust. Sci. 38 (5), 630–671.
Ryden, M., Lyngfelt, A., 2006. Using steam reforming to produce hydrogen with carbon dioxide capture by chemical-looping combustion. Int. J. Hydrogen Energy 31 (10), 1271–1283.
Ryden, M., Lyngfelt, A., Mattisson, T., 2006. Synthesis gas generation by chemical-looping reforming in a continuously operating laboratory reactor. Fuel 85 (12-13), 1631–1641.
Rydén, M., et al., 2008. Novel oxygen-carrier materials for chemical-looping combustion and chemical-looping reforming; LaxSr1 − xFeyCo1 − yO3 − δ perovskites and mixed-metal oxides of NiO, Fe2O3 and Mn3O4. Int. J. Greenh. Gas Control. 2 (1), 21–36.
Spallina, V., et al., 2017. Chemical looping reforming in packed-bed reactors: modelling, experimental validation and large-scale reactor design. Fuel Process. Technol. 156, 156–170.
Tong, A., et al., 2013. Application of the moving-bed chemical looping process for high methane conversion. Energy Fuels 27 (8), 4119–4128.
Viebahn, P., Vallentin, D., Holler, S., 2015. Prospects of carbon capture and storage (CCS) in China's power sector - an integrated assessment. Appl. Energy 157, 229–244.
Wassie, S.A., et al., 2017. Hydrogen production with integrated CO2 capture in a novel gas switching reforming reactor: proof-of-concept. Int. J. Hydrogen Energy 42 (21), 14367–14379.
Wassie, S.A., et al., 2018. Hydrogen production with integrated CO2 capture in a membrane assisted gas switching reforming reactor: proof-of-Concept. Int. J. Hydrogen Energy 43 (12), 6177–6190.
Wechsler, B.A., Lindsley, D.H., Prewitt, C.T., 1984. Am. Mineral. 69, 754–770.
Zaabout, A., et al., 2013. Experimental demonstration of a novel gas switching combustion reactor for power production with integrated CO2 capture. Ind. Eng. Chem. Res. 52 (39), 14241–14250.
Zaabout, A., Cloete, S., van Sint Annaland, M., Gallucci, F., Amini, S., 2015. A novel gas switching combustion reactor for power production with integrated CO_2 capture: Sensitivity to the fuel and oxygen carrier types. Int. J. Greenh. Gas Control 39, 185–193.
Zaabout, A., Cloete, S., Amini, S., 2016. Innovative internally circulating reactor concept for chemical looping-based CO_2 capture processes: Hydrodynamic investigation. Chem. Eng. Technol. 39 (8), 1413–1424.
Zaabout, A., Cloete, S., Amini, S., 2017. Autothermal operation of a pressurized Gas Switching Combustion with ilmenite ore. International Journal of Greenhouse Gas Control 63, 175–183.
Zafar, Q., Mattisson, T., Gevert, B., 2006. Redox investigation of some oxides of transition-state metals Ni, Cu, Fe, and Mn supported on SiO2 and MgAl2O4. Energy & Fuels 20 (1), 34–44.
Zheng, Y., et al., 2017. Designed oxygen carriers from macroporous LaFeO3 supported CeO2 for chemical-looping reforming of methane. Appl. Catal. B: Environ. 202, 51–63.
Zhou, Z., Han, L., Bollas, G.M., 2013. Model-based analysis of bench-scale fixed-bed units for chemical-looping combustion. Chem. Eng. J. 233, 331–348.
Zhu, X., et al., 2014. Chemical-looping steam methane reforming over a CeO2-Fe2O3 oxygen carrier: evolution of its structure and reducibility. Energy Fuels 28 (2), 754–760.